JACS
JOURNAL OF THE AMERICAN CHEMICAL SOCIETY

Article

pubs.acs.org/JACS

Metal–Organic-Framework-Derived Co–Fe Bimetallic Oxygen Reduction Electrocatalysts for Alkaline Fuel Cells

Yin Xiong,[#] Yao Yang,[#] Francis J. DiSalvo, and Héctor D. Abruña*

Department of Chemistry and Chemical Biology, Baker Laboratory, Cornell University, Ithaca, New York 14853, United States

Supporting Information

ABSTRACT: The oxygen reduction reaction (ORR) is considered the cornerstone for regenerative energy conversion devices involving fuel cells and electrolyzers. The development of non-precious-metal electrocatalysts is of paramount importance for their large-scale commercialization. Here, Co–Fe binary alloy embedded bimetallic organic frameworks (BMOF)s based on carbon nanocomposites have been designed with a compositionally optimized template, by a facile host–guest strategy, for ORR in alkaline media. The electrocatalyst exhibits promising electrocatalytic activity for ORR with a half-wave potential of 0.89 V in 0.1 M NaOH, comparable to state-of-the-art Pt/C electrocatalysts. More importantly, it exhibits robust durability after 30 000 potential cycles. Scanning transmission electron microscopy (STEM) and quantitative energy-dispersive X-ray (EDX) spectroscopy suggest that the Co–Fe alloy nanoparticles have a homogeneous elemental distribution of Co and Fe at the atomic-scale optimized BMOF and Co/Fe ratio of 9:1. The long-term durability is attributed to its ability to maintain its structural and compositional integrity after the cycling process, as evidenced by STEM-EDX analysis. This work provides valuable insights into the design and fabrication of novel platinum-group-metals-free highly active ORR electrocatalysts in alkaline media.

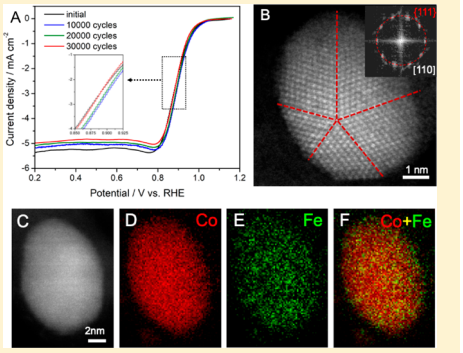

INTRODUCTION

The continuing consumption of nonrenewable fossil fuels and increased aspiration for a global sustainable energy technology landscape has stimulated the development of novel fuel cell technologies.[1,2] The regenerative energy conversion concept, targeting low-carbon or carbon-free fuels, makes it a promising approach to lower CO_2 emissions.[3,4] The challenge to accelerate the sluggish oxygen reduction reaction (ORR) at the cathode in fuel cell applications will require novel materials and architectures. Platinum-group-metals (PGM)-based materials are still considered to be the state-of-the-art electrocatalysts toward the ORR.[5−7] However, their large-scale application in fuel cells is still precluded by cost and limited stability.[8,9] Thus, there is a clear need to design and develop cost-effective alternatives with high electrocatalytic activity and robust long-term stability. Alkaline polymer electrolyte fuel cells (APEFCs) have attracted a great deal of interest in the recent past because they can enable the use of non-precious metals as electrocatalysts for the ORR.[10] In this context, extensive investigations have focused on non-PGM materials, including transition-metal oxide,[11−18] ranging from monometallic to trimetallic oxides, and PGM-free nitrogen-doped carbon materials.[19−21] Dai and co-workers reported on Mn–Co oxides loaded on N-doped reduced graphene oxide, which significantly enhanced the electrocatalytic activity by the covalent coupling effect between the support and the oxide nanoparticles.[22] Yang et al. studied perovskite-based oxides, applying them for both oxygen reduction and evolution reactions.[23] Zelenay and Dodelet have utilized nitrogen-containing organic molecules incorporating earth-abundant Co or Fe, to prepare metal–nitrogen–carbon (M–N–C) materials through high-temperature pyrolysis. The resulting materials have exhibited promising performance in membrane electrode assemblies (MEAs), providing further impetus to the industrial application of PGM-free electrocatalyst materials.[24−27] Furthermore, Lu et al., Peng et al., and Sa et al. have fabricated a variety of non-PGM catalysts, including carbonaceous material derived from halloysite, CoO_x nanohybrids, and Fe–N-doped carbon materials, respectively. They are adapted in APEFCs and demonstrated excellent performance.[28−30]

Recently, metal–organic frameworks (MOFs) (containing metal centers and organic linkers) have generated a great deal of attention as scaffolds and precursors for novel families of carbon nanocomposites.[31,32] As representatives of MOFs, zeolitic imidazolate frameworks (ZIFs) such as ZIF-67 and ZIF-8, with available metal centers and highly abundant carbon and nitrogen, have emerged as promising precursors as electrocatalysts.[33,34] The nitrogen species can bond to non-noble-metal nanoparticles as a means to yield N-doped carbon materials.[35] Nitrogen atoms can generate positively charged sites that are conducive to O_2 adsorption or splitting, which is believed to help expedite the kinetics of the oxygen reduction reaction.[36,37] There have been numerous reports on these contexts. Lou and co-workers employed ZIF-67 to produce

Received: April 6, 2019
Published: June 19, 2019

DOI: 10.1021/jacs.9b03561
J. Am. Chem. Soc. XXXX, XXX, XXX−XXX

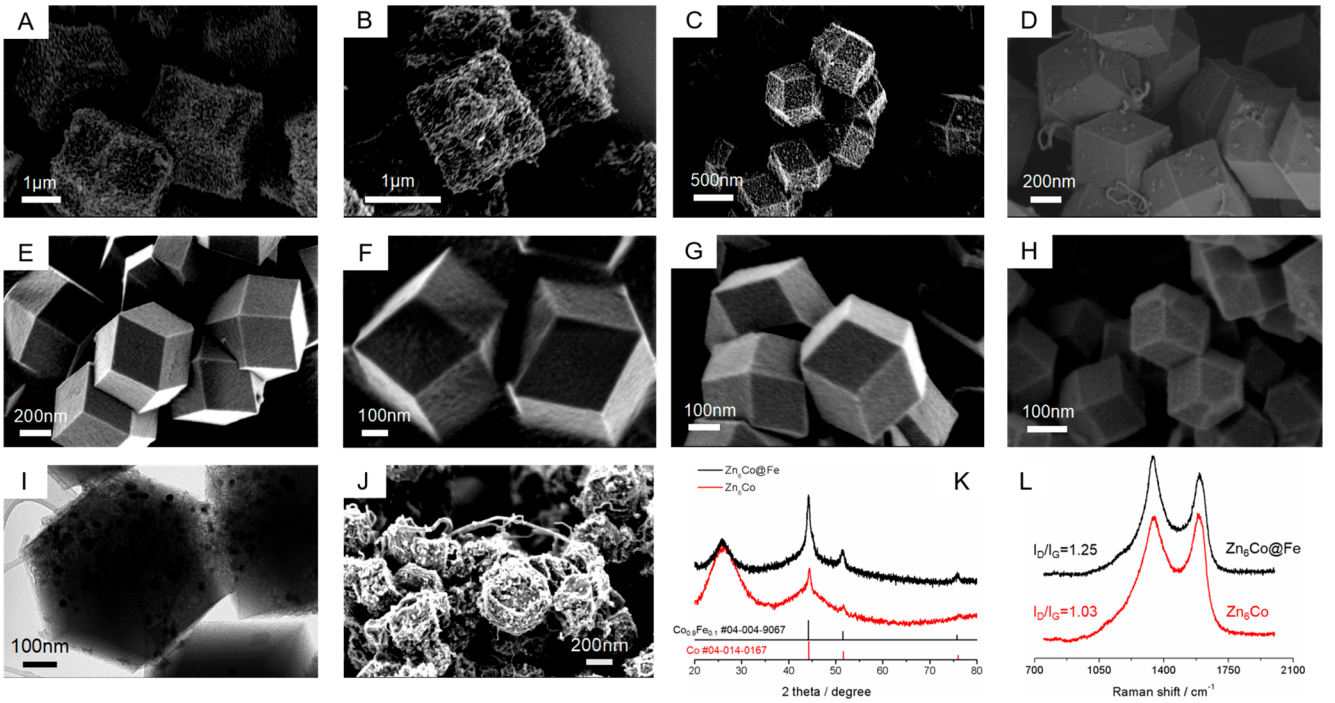

Figure 1. (A–H) SEM images of pyrolyzed BMOF_Co, BMOF_$ZnCo_3$, BMOF_ZnCo, BMOF_Zn_3Co, BMOF_Zn_6Co, BMOF_$Zn_{11}Co$, BMOF_$Zn_{20}Co$, and BMOF_Zn at 800 °C in forming gas (95% N_2 and 5% H_2). (I) TEM image of the pyrolyzed Zn_6Co. (J) SEM image of the pyrolyzed Zn_6Co_Fe. (K) XRD patterns of Zn_6Co and Zn_6Co_Fe. (L) Raman spectrum of Zn_6Co and Zn_6Co_Fe.

porous hollow carbon polyhedra, comprised of N-doped carbon nanotubes (CNTs), as bifunctional electrocatalysts toward the ORR and OER.[38] Song and co-workers used ZIF-8 as a sacrificial framework that was pyrolyzed and activated with NH_3 for optimized N configuration/doping to boost electrocatalytic activity.[39] ZIF-67-derived materials feature N-doped mesoporous graphitic carbon with a stable structure, as well as high electronic conductivity and Co decoration for the generation of active sites. ZIF-8 provides a hollow framework with high surface area, promoting rapid diffusion kinetics during electrocatalysis. Jiang and co-workers, Su and co-workers, and others have employed bimetallic mixtures of ZIF-67 and ZIF-8 as templates, further doped with phosphate anions, to fabricate electrocatalytically active nanocarbon materials after pyrolysis in Ar.[40,41]

Herein, we report on a group of optimized bimetallic MOFs (BMOFs) derived from a Co–Fe alloy embedded in a carbon nanocomposite, which when compositionally optimized, exhibits highly stable electrocatalytic activity toward the ORR. In ZIF-8, volatile Zn metal centers can evaporate, generating a carbon structure with high surface area and porosity. The resulting cavities served as hosts to encapsulate Fe ions to form a Co–Fe alloy with cobalt derived from the ZIF-67 or with externally added $Fe(acac)_3$. The resulting nanocomposite exhibited ORR electrocatalytic activity comparable to commercial Pt, as well as high stability for the ORR in alkaline media as evidenced by its compositional and structural integrity.

RESULTS AND DISCUSSION

A family of Co–Zn bimetallic MOFs (BMOFs) precursors were synthesized by a facile one-step solvothermal method at room temperature, through the self-assembly of Co^{2+}/Zn^{2+} with 1,2-methyimidazole in a solvent mixture of ethanol and methanol. Their compositions were varied systematically and labeled as BMOF-Co, $ZnCo_3$, ZnCo, Zn_3Co, Zn_6Co, $Zn_{11}Co$, $Zn_{20}Co$, and Zn, representing the fraction of the Co^{2+} salt ($Co(NO_3)_2$) as 100%, 75%, 50%, 14%, 8%, 5%, and 0%, respectively. The powder X-ray diffraction (XRD) patterns of the resulting BMOFs are shown in Figure S1 (Supporting Information), where those of BMOF_Co and Zn were consistent with the simulated XRD patterns of ZIF-67 and ZIF-8, respectively. The intermediate XRD patterns were analogous to ZIF-67 and ZIF-8, indicating the successful synthesis of the BMOFs. Their morphologies were characterized via scanning electron microscopy (SEM) and transmission electron microscopy (TEM), shown in Figures S2 and S3, indicating a uniform distribution and smooth surfaces. The BMOF crystal sizes decreased at higher Zn/Co ratios in the metal precursors with less metallic Co nanoparticles remaining. The crystal size decreased from the BMOF_Co sample, with an average edge length of around 2 μm, to around 1 μm in BMOF_ZnCo, and eventually to <100 nm in BMOF_Zn. As expected, there exists a correlation between the diminution in the crystal size and the increasing fraction of Co in the salt precursors. The formed polyhedra were pyrolyzed under forming gas at 800 °C for 2 h, followed by a sulfuric acid wash to remove any leachable metallic Co. As shown in Figure 1A–H, the polyhedral morphology of the crystals was retained after the heat treatment and acid wash. It is generally accepted that CNTs (carbon nanotubes) would likely grow on most transition metals at elevated temperatures and under a sufficiently high H_2 pressure.[42] The nanocomposites with higher Co content yielded rougher surfaces, suggesting the formation of a higher amount of carbon nanotubes. Figure S4 shows the XRD patterns of the carbonized BMOFs in which all materials exhibited two peaks at 25° and 44° indexed to the (002) and (101) peaks of carbon, and XRD peaks at 44° and

DOI: 10.1021/jacs.9b03561
J. Am. Chem. Soc. XXXX, XXX, XXX–XXX

51° ascribed to the (111) and (200) peaks of metallic Co in a face-centered cubic structure. At higher Co contents, metallic Co peaks became more pronounced. The generated Zn oxide was expected to be reduced in the forming gas atmosphere or by carbon, which subsequently vaporized at high temperature. Thus, there were no diffraction peaks from Zn. The thermogravimetric analysis measurements in Figure S5A were used to confirm the complete removal of Zn. The residual mass of pyrolyzed BMOFs was precisely proportional to the amount of Co precursors, and the Co-free material had nearly a 100% mass loss after acid leaching. The BMOF material derived from the Zn_6Co composite was further used as the scaffold to encapsulate the Fe^{3+} in its cavities/pores via the double-solvent method.[43,44] The Fe^{3+} moieties were immobilized in the pores of the Zn_6Co network and reduced simultaneously with their neighboring Co atoms, creating the bimetallic active sites after carbonization and acid leaching.

Figure S6A,B shows the morphology of BMOF_Zn_6Co before and after thermal treatment and acid leaching, confirming that neither of the two processes affected the overall morphology. The TEM image of the pyrolyzed BMOF_Zn_6Co in Figure 1I demonstrates that the polyhedral scaffold of carbon was embedded with metallic Co nanoparticles. With the incorporation of Fe, the resulting carbon nanocomposite, derived from Zn_6Co (labeled as Zn_6Co_Fe), had abundant carbon nanotubes, covering the surface of the polyhedral crystals (Figure 1J). The XRD patterns of pyrolyzed Zn_6Co and Zn_6Co_Fe revealed that metallic Co and bimetallic $Co_{0.9}Fe_{0.1}$ were formed in the reducing atmosphere during carbonization and were retained after the acid wash. The diffraction pattern of the pyrolyzed Zn_6Co_Fe in Figure 1K exhibited a slight shift to lower angles compared to the non-Fe counterpart, consistent with the larger atomic radius of Fe. There were two peaks observed in the Raman spectrum shown in Figure 1L, illustrating the D and G band features of carbon. The Raman peaks located at 1350 and 1600 cm^{-1} were attributed to sp^2 graphite and defects in the carbon, respectively.

The defects could come from the heteroatom substitution, vacancies, and grain boundaries, which are commonly considered to be more active in electrocatalysis than the basal plane.[45] The D/G band ratio increased from 1.03 to 1.25 after the addition of Fe, indicating the formation of more defect sites facilitating electrocatalysis. It was speculated that the volatile Zn would substantially increase the surface area. The BET surface areas of four representative samples, the carbon nanocomposites from Co, Zn_6Co, Zn and Zn_6Co_Fe were measured to be 520, 1310, 1400, and 745 m^2/g, respectively. The high surface area allowed the exposure of active sites and was deemed beneficial to the rapid transport of O_2 and relevant species during the electrocatalysis processes (Figure S5B).

The atomic structure of the $Co_{0.9}Fe_{0.1}$, embedded in the carbon nanocomposite, derived from Zn_6Co_Fe, was further examined by high-angle annular dark-field (HAADF) scanning transmission electron microscopy (STEM) imaging. Because STEM image intensity is proportional to the atomic number ($I \propto Z^{1.7}$), the $Co_{0.9}Fe_{0.1}$ alloy particles will be significantly brighter than the carbon support. As shown in Figure 2A, $Co_{0.9}Fe_{0.1}$ bimetallic nanoparticles (NPs) were uniformly distributed and embedded in the MOF-derived porous carbon matrix. $Co_{0.9}Fe_{0.1}$ NPs exhibited narrow particle size distribution (PSD) of 8 ± 2 nm (average ± one standard deviation, S_d) (Figure 2B) on the basis of an analysis of more than 300 nanoparticles from Figure 2A and Figure S7. The crystal structure was further examined by STEM images at the atomic scale. Figure 2C shows a single-crystal nanoparticle with a *d*-spacing value of 0.20 nm, which is consistent with the theoretical radius of $Co_{0.9}Fe_{0.1}$ {111} facets, 0.2048 nm (PDF # 04-004-9067). Another $Co_{0.9}Fe_{0.1}$ nanoparticle was found to have five subdomains of {111} *d*-spacings on the same zone

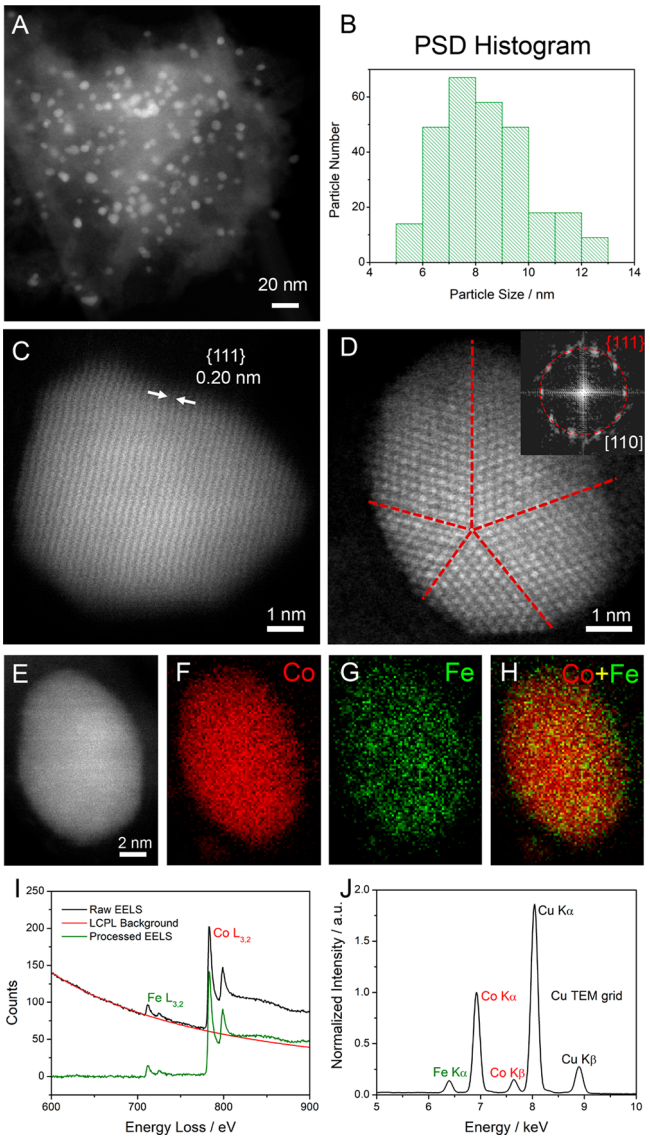

Figure 2. HAADF-STEM images of $Co_{0.9}Fe_{0.1}$ bimetallic nanoparticles embedded in a MOF-derived porous carbon matrix (BMOF). (A) low-magnification STEM image of BMOF. (B) Particle size distribution (PSD) histogram of about 300 particles analyzed from (A) and Figure S4. (C) Atomic-scale STEM image of a single crystal with a *d*-spacing value of 0.20 nm, indicating {111} facets of $Co_{0.9}Fe_{0.1}$. (D) Atomic-scale STEM image of a nanoparticle with five subdomains on the [110] zone axis and the domain boundaries indicated as the red dashed lines. Inset shows the corresponding Fourier transform with five pairs of {111} diffraction spots; chemical composition of a $Co_{0.9}Fe_{0.1}$ bimetallic nanoparticle. (E–H) STEM image and the corresponding EELS elemental maps of Co (red), Fe (green), and the composite map (Co vs Fe). (I) Processed EELS spectrum with pronounced Fe and Co $L_{3,2}$ edges. (J) STEM-EDX spectrum with Fe Kα and Co Kα,β edges. Quantitative EDX analysis suggests Fe and Co contents of 89.2 and 10.8 at. %, respectively.

DOI: 10.1021/jacs.9b03561
J. Am. Chem. Soc. XXXX, XXX, XXX−XXX

axis of [110] (Figure 2D and Figure S8). Domain boundaries were marked with red dashed lines, and the hexagonal symmetry of [110] in each domain was clearly resolved from the atom arrangements. The Fourier transform of this nanoparticle showed the corresponding five pairs of diffraction spots with the same *d*-spacing values, as indicated by the dashed red circle (Figure 2D inset). The energy loss spectroscopy (EELS) and energy-dispersive X-ray spectroscopy (EDX) (Figure 2I) show the pronounced Co and Fe $L_{3,2}$ edges at around 790 and 710 eV, respectively, which were used to extract 2D EELS elemental mapping. Figure 2E,F presents a 10 nm $Co_{0.9}Fe_{0.1}$ nanoparticle with EELS maps of Co (red) and Fe (green). The EELS composite map of Co vs Fe in the upper right of Figure 2E,F suggested a relatively homogeneous distribution of Co and Fe, which was further evidenced by similar EELS maps in Figure S9. This provides convincing and compelling evidence of the formation of a Co−Fe alloy at the atomic scale, which is consistent with the observation from the XRD of $Co_{0.9}Fe_{0.1}$ in Figure 2K. Besides the elemental distribution from EELS, EDX also served as a quantitative tool to analyze the local atomic ratio (Figure 2J). Co and Fe Kα edges at 6.9 and 6.4 keV, respectively, were employed to calculate the relative atomic contents of Fe and Co on the basis of the Cliff-Lorimer equation.[46] Co and Fe were found to have relative contents of 89.2% and 10.8%, respectively, which is consistent with the designed stoichiometry of Co/Fe (9:1) and ICP-MS results, which indicated that the atomic ratio of Co to Fe was around 9:1. The relative error was defined as one S_d of 0.6% on the basis of a random selection of five different regions on the TEM grid. The strong Cu signal in Figure 2J came from the Cu TEM grid. STEM-EDX elemental maps of several $Co_{0.9}Fe_{0.1}$ NPs also yielded similar homogeneous distribution of Co and Fe to that obtained from EELS mapping (Figure S10). In summary, microscopic-level STEM-EELS mapping, combined with quantitative EDX analysis, unambiguously indicate that the $Co_{0.9}Fe_{0.1}$ alloy nanoparticles have a homogeneous distribution of Co and Fe at the atomic scale with the designed Co/Fe ratio of 9:1.

With the desirable structural information discussed above, the electrocatalytic performance of these materials, toward the ORR, was assessed in alkaline media. Shown in Figure 3A, all the polarization curves of all BMOFs-derived carbon nanocomposites were collected in a conventional three-electrode system at 1600 rpm, in an O_2-saturated 0.1 M NaOH electrolyte, at a scan rate of 5 mV/s and a rotation rate of 1600 rpm. The mass activities at 0.85 V and the half-wave potentials are summarized in Figure 3B. The Zn-derived material showed the lowest onset potential and the slowest kinetics in the mixed diffusion-kinetics control region. In sharp contrast, with a minimal amount of Co incorporated, the electrocatalytic performance of the $Zn_{20}Co$-derived sample had a dramatically enhanced increase of 200% in mass activity and a 30 mV positive shift in the half-wave potential. This dramatic improvement indicated that Co provided critical active sites for ORR electrocatalysis. With additional increases in the Co loading, there were further increases in the mass activity, although the additional relative enhancement gradually decreased with higher Co contents. Contrary to such behavior, in the case of Zn_6Co to Co, the electrocatalytic activity decreased with increasing levels of Co. As a result, Zn_6Co proved to be the best ORR candidate derived from BMOFs precursors. We ascribe this to its high surface area, accessible Co-based active sites, and N dopants. Furthermore, the Co−Fe

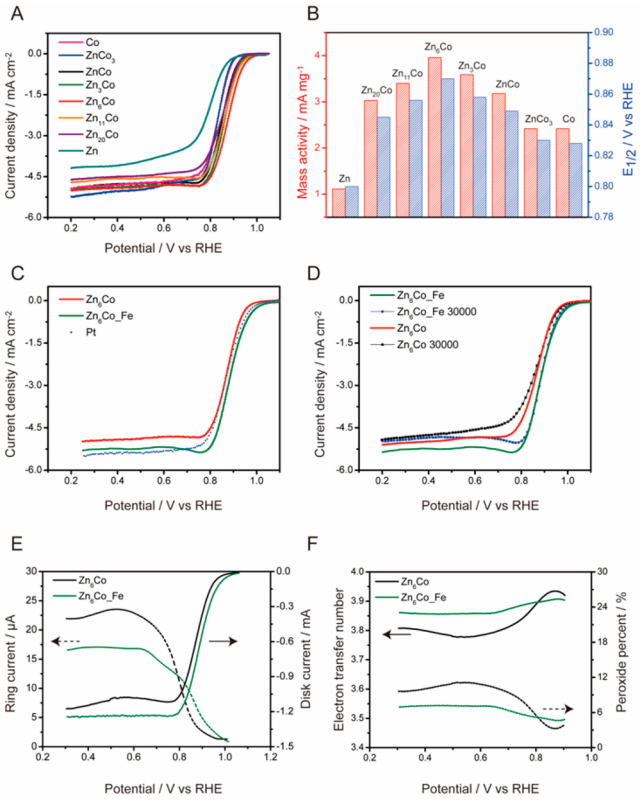

Figure 3. Oxygen reduction on pyrolyzed BMOFs and Zn_6Co_Fe. (A) Polarization curves of a variety of BMOFs samples obtained in O_2-saturated 0.1 M NaOH at 1600 rpm and a scan rate of 5 mV/s. (B) Comparison of the mass activity at 0.85 V and half-wave potentials ($E_{1/2}$). (C) Polarization curves of pyrolyzed Zn_6Co, Zn_6Co_Fe, and commercial Pt. (D) Polarization curves of Zn_6Co and Zn_6Co_Fe before and after 30 000 cycles. (E) Rotating ring-disk electrode (RRDE) measurements of Zn_6Co and Zn_6Co_Fe in 0.1 M NaOH toward ORR. Ring and disk currents obtained at 1600 rpm and 5 mV/s. (F) Calculated electron transfer number and peroxide yield.

bimetallic alloy derived from Zn_6Co, namely, Zn_6Co_Fe, exhibited electrocatalytic activity that surpassed those of Zn_6Co and commercial Pt/C, in terms of the half-wave potential (Figure 3C).

Stability was assessed for carbon nanocomposites derived from both Zn_6Co and Zn_6Co_Fe in an Ar-saturated 0.1 M NaOH solution at a scan rate of 100 mV/s for 30 000 cycles (Figure 3D), where the carbon derived from Zn_6Co_Fe proved extraordinarily stable. After 30 000 CV cycles, there was virtually no loss in the potential region between 0.8 and 1.0 V, and the electrocatalytic activity still outperformed that of Zn_6Co carbon. To better evaluate the selectivity of the oxygen reduction process, the rotating ring-disk electrode (RRDE) method was employed to measure the peroxide yield, corresponding to the undesirable $2e^-$ process. Figure 3E presents the ring and disk currents obtained for Zn_6Co and Zn_6Co_Fe. Zn_6Co_Fe exhibited a higher disk current, while its ring current decreased by 30%, when compared to Zn_6Co, suggesting a dominant four-electron transfer reaction. The electron transfer number (n) and peroxide yield values are presented in Figure 3F. For the Zn_6Co_Fe carbon, the n-value was determined to be above 3.9 over the potential region between 0.2 and 0.9 V, and the generated peroxide was below 7%, a value that is about half, when compared to the 12%

DOI: 10.1021/jacs.9b03561
J. Am. Chem. Soc. XXXX, XXX, XXX−XXX

H_2O_2 generation from Zn_6Co. The peroxide yield is relatively low when compared to other reported values in the literature. Our results are, in fact, comparable to other state-of-the-art catalysts. To make a better comparison, we have prepared a table that summarizes the peroxide yield of various materials in Table S1.[28−30,47−55] Lowering the peroxide yield would be most beneficial because it is well understood that peroxide can diffuse into the membrane and chemically break down to hydroxyl radicals. These radicals, in return, will react with perfluorosulfonic ionomers in the electrode and the membrane to produce hydrofluoric acid (HF), leading to the degradation of the MEA.[56] To address the disadvantage from produced peroxide, it requires collaborative efforts, also from the design of peroxide-tolerant membranes.[57]

To implement Pt-free cathodes for industrial applications in alkaline membrane exchange fuel cells (AMEFCs), non-precious ORR electrocatalysts need to not only satisfy the requirements of high initial ORR activity but also address long-term durability concerns.[58] The durability and the possible degradation mechanisms of ORR electrocatalysts need to satisfy the requirements of the BMOF electrocatalysts that were investigated using STEM imaging and quantitative EDX analysis. As shown in Figure 4A, the half-wave potentials of

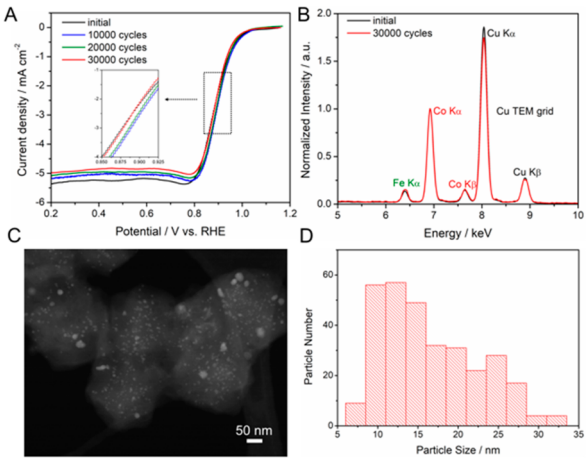

Figure 4. Degradation mechanism investigation of BMOF electrocatalysts during durability tests. (A) ORR polarization profiles of BMOF electrocatalysts at 1600 rpm and 5 mV/s after 10 000, 20 000, and 30 000 potential cycles from 0.6 to 1.0 V at 100 mV/s. (B) EDX spectra of BMOF at the initial state and after 30 000 cycles, showing a relatively stable Fe/Co atomic ratio. (C) STEM image of BMOF after 30 000 cycles, showing a majority of small particles as well as aggregated larger particles. (D) PSD histogram of BMOF after 30 000 cycles, analyzed from (C) and Figure S8, showing an increasing number of larger particles, relative to the initial state in Figure 3B.

BMOF electrocatalysts shifted slightly positively after 10 000 and 20 000 cycles, indicating an initial catalyst activation. After 30 000 cycles, the $E_{1/2}$ shifted in the negative direction by less than 5 mV, indicating a remarkable activity retention. The continuous decrease in I_d from −5.4 to −5.0 mA/cm^2 suggests a loss of electrochemical surface area (ECSA). EDX quantitative analysis and STEM images were employed to investigate the changes in microstructures and local chemical composition. EDX spectra of BMOF electrocatalysts, at the initial state and after 30 000 cycles, were normalized to the Co Kα edge (783 eV) and showed little, if any, changes in the Fe Kα edge (712 eV) (Figure 4B). Quantitative analysis suggested that the relative contents of Co and Fe changed from 89.2% and 10.8% (±0.6%) at the initial state to 88.5% and 11.5% (±0.8%) after 30 000 cycles, respectively. Given the relative error of EDX measurements, no significant changes in composition ratio were detected. STEM images of BMOF electrocatalysts after 30 000 cycles showed that the majority of the small particles were able to remain embedded in the carbon matrix with only a few aggregated larger particles evident (Figure 4C). Around 300 $Co_{0.9}Fe_{0.1}$ nanoparticles in Figure 4C and Figure S11 were analyzed to form the particle size distribution (PSD) histogram in Figure 4D. It suggests that $Co_{0.9}Fe_{0.1}$ NPs have a larger average particle size of 10−15 nm and a broader PSD after 30 000 cycles, when compared to the initial state in Figure 2, which may partially explain the decrease in I_d in Figure 4A. Initially, nearly all O_2 could be fully reduced to H_2O via either direct four-electron transfer reaction or in a two-step process in which the generated peroxide is fully reduced (to water) by nearby sites before escaping the catalyst layer. After potential cycling process, some active sites dissolved so that their density is lower. In this case, the peroxide has a higher possibility of diffusing into the bulk electrolyte, causing a decrease in the limiting current. The $E_{1/2}$ does not shift too much in the kinetic-diffusion region, indicating that the kinetics is relatively fast. In summary, the excellent durability of BMOF-derived electrocatalysts after 30 000 cycles was ascribed to their capability to maintain a stable local chemical composition as well as a reasonably small particle size, highlighting the close interactions between $Co_{0.9}Fe_{0.1}$ NPs and the MOF-derived carbon matrix. Here, we attributed the stability of our Co−Fe BMOF catalysts to the highly porous structure arising from the use of Zn as a sacrificial template in the reducing atmosphere and to the in situ formation of the Co−Fe bimetallic nanoparticles. The annealing processes was deliberately conducted at H_2 flowing rates, known to promote the formation of carbon nanotubes on the surface of transition metals, like Co and Fe in this case, that help immobilize active sites. At the same time, Co and Fe are reduced and alloyed at the elevated temperatures employed during the formation of these CNTs and are subsequently wrapped in these tubes. In addition, the 1,2-immidazole ligands in the BMOF precursors bring N dopants in the carbon structure, which are able to not only provide additional catalytic pathways but also bind and coordinate the metallic nanoparticles, thus enhancing stability from both chemical and physical prospective. The porous structure of our materials is maintained after extensive cycling, as evidenced by TEM. Together with the minimal compositional difference between a fresh sample and a sample after 30 000 cycles, it is reasonable to expect that the excellent stability derives from the structural and chemical integrity.

In addition, based on the Pourbaix diagram, the surface of the bimetallic Co−Fe nanoparticle is highly likely to be partially oxidized, in the form of Co and Fe oxide/hydroxide. It is possible/likely that, under working conditions (applied potential), there is a mixture of $Co(OH)_2$ and $Co(OH)_3$ (or Co_2O_3, Co_3O_4, and CoO) for Co on the surface. Similarly, Fe likely exists as a mixture of $Fe(OH)_2$ and $Fe(OH)_3$ (or Fe_2O_3 and Fe_3O_4). The average valence state is likely to be potential-dependent, closer to +3 in the higher potential region (near 1 V vs RHE) and near +2 when the applied potential is lower (near 0 V vs RHE). Those two metals on the surface simultaneously and synergistically catalyze the ORR reaction efficiently and stably.

DOI: 10.1021/jacs.9b03561
J. Am. Chem. Soc. XXXX, XXX, XXX−XXX

CONCLUSIONS

In summary, we have designed a family of BMOF-derived Co–Fe alloys embedded in a carbon nanocomposite through the combination of the conventional self-assembly of MOFs and a guest–host strategy. Zn_6Co proved to be the compositionally optimized template and substrate for the encapsulation of exterior Fe to generate the bimetallic nanoparticles–carbon composite. This nanocomposite, composed of porous carbon with high surface area and uniform distribution of $Co_{0.9}Fe_{0.1}$ bimetallic nanoparticles, exhibited superior electrocatalytic activity toward the ORR, as well as robust stability after 30 000 cycles, owing to its structural and compositional integrity, as confirmed by STEM and EDX measurement. The synthesis strategy and optimization process presented here may provide new pathways to push forward the substitution of Pt with more cost-effective electrocatalysts for fuel cell applications.

ASSOCIATED CONTENT

Supporting Information

The Supporting Information is available free of charge on the ACS Publications website at DOI: 10.1021/jacs.9b03561.

Synthesis, structural characterizations of XRD, BET, SEM, and TEM, and additional figures (PDF)

AUTHOR INFORMATION

Corresponding Author

*hda1@cornell.edu

ORCID

Yao Yang: 0000-0003-0321-3792

Héctor D. Abruña: 0000-0002-3948-356X

Author Contributions

#Y.X. and Y.Y. contributed equally to this work.

Notes

The authors declare no competing financial interest.

ACKNOWLEDGMENTS

This work was supported by the Center for Alkaline-Based Energy Solutions (CABES) and the Center for Energy Materials at Cornell (emc^2), part of the Energy Frontier Research Center (EFRC) program supported by the U.S. Department of Energy, under grant DE-SC-0019445. Y.X. and Y.Y. are funded by DOE under the grant DE-SC-0019445. This work made use of TEM facilities at the Cornell Center for Materials Research (CCMR) which are supported through the National Science Foundation Materials Research Science and Engineering Center NSF MRSEC program (DMR-1719875). We are grateful to Malcolm (Mick) Thomas at CCMR for help in Nion UltraSTEM.

REFERENCES

(1) Chu, S.; Majumdar, A. *Nature* **2012**, *488*, 294.

(2) Xiong, Y.; Yang, Y.; Joress, H.; Padgett, E.; Gupta, U.; Yarlagadda, V.; Agyeman-Budu, D.; Huang, X.; Moylan, T. E.; Zeng, R.; Kongkanand, A.; Escobedo, F. A.; Brock, J. D.; DiSalvo, F. J.; Muller, D. A.; Abruña, H. D. *Proc. Natl. Acad. Sci. U. S. A.* **2019**, *116*, 1974.

(3) Dresselhaus, M.; Thomas, I. *Nature* **2001**, *414*, 332.

(4) Dunn, B.; Kamath, H.; Tarascon, J. *Science* **2011**, *334*, 928.

(5) Kongkanand, A.; Mathias, M. *J. Phys. Chem. Lett.* **2016**, *7*, 1127.

(6) Xiong, Y.; Yang, Y.; DiSalvo, F. J.; Abruña, H. D. *J. Am. Chem. Soc.* **2018**, *140*, 7248.

(7) Xiong, Y.; Xiao, L.; Yang, Y.; DiSalvo, F. J.; Abruña, H. D. *Chem. Mater.* **2018**, *30*, 1532.

(8) Meier, J.; Katsounaros, I.; Galeano, C.; Bongard, H.; Topalov, A.; Kostka, A.; Karschin, A.; Schüth, F.; Mayrhofer, K. *Energy Environ. Sci.* **2012**, *5*, 9319.

(9) Liu, X.; Park, M.; Kim, M.; Gupta, S.; Wu, G.; Cho, J. *Angew. Chem., Int. Ed.* **2015**, *54*, 9654.

(10) Wang, Y.; Qiao, J.; Baker, R.; Zhang, J. *Chem. Soc. Rev.* **2013**, *42*, 5768.

(11) Yang, Y.; Wang, Y.; Xiong, Y.; Huang, X.; Shen, L.; Huang, R.; Wang, H.; Pastore, J. P.; Yu, S.-H.; Xiao, L.; Brock, J. D.; Zhuang, L.; Abruña, H. D. *J. Am. Chem. Soc.* **2019**, *141*, 1463.

(12) Xiong, Y.; Yang, Y.; Feng, X.; DiSalvo, F. J.; Abruña, H. D. *J. Am. Chem. Soc.* **2019**, *141* (10), 4412.

(13) Wang, J.; Cui, W.; Liu, Q.; Xing, Z.; Asiri, A.; Sun, X. *Adv. Mater.* **2016**, *28*, 215.

(14) Zhu, Y.; Ma, T.; Jaroniec, M.; Qiao, S. *Angew. Chem., Int. Ed.* **2017**, *56*, 1324.

(15) Cheng, F.; Shen, J.; Peng, B.; Pan, Y.; Tao, Z.; Chen, J. *Nat. Chem.* **2011**, *3*, 79.

(16) Jiao, F.; Frei, H. *Angew. Chem., Int. Ed.* **2009**, *48*, 1841.

(17) Yeo, B.; Bell, A. *J. Am. Chem. Soc.* **2011**, *133*, 5587.

(18) Li, T.; Xue, B.; Wang, B.; Guo, G.; Han, D.; Yan, Y.; Dong, A. *J. Am. Chem. Soc.* **2017**, *139*, 12133.

(19) Ren, H.; Wang, Y.; Yang, Y.; Tang, X.; Peng, Y.; Peng, H.; Xiao, L.; Lu, J.; Abruña, H. D.; Zhuang, L. *ACS Catal.* **2017**, *7*, 6485.

(20) Gong, K.; Du, F.; Xia, Z.; Durstock, M.; Dai, L. *Science* **2009**, *323*, 760.

(21) Liang, H.; Wei, W.; Wu, Z.; Feng, X.; Müllen, K. *J. Am. Chem. Soc.* **2013**, *135*, 16002.

(22) Liang, Y.; Wang, H.; Zhou, J.; Li, Y.; Wang, J.; Regier, T.; Dai, H. *J. Am. Chem. Soc.* **2012**, *134*, 3517.

(23) Suntivich, J.; Gasteiger, H.; Yabuuchi, N.; Nakanishi, H.; Goodenough, J.; Shao-Horn, Y. *Nat. Chem.* **2011**, *3*, 546.

(24) Wu, G.; More, K.; Johnston, C.; Zelenay, P. *Science* **2011**, *332*, 443.

(25) Chung, H.; Cullen, D.; Higgins, D.; Sneed, B.; Holby, E.; More, K.; Zelenay, P. *Science* **2017**, *357*, 479.

(26) Proietti, E.; Jaouen, F.; Lefèvre, M.; Larouche, N.; Tian, J.; Herranz, J.; Dodelet, J. *Nat. Commun.* **2011**, *2*, 416.

(27) Lefèvre, M.; Proietti, E.; Jaouen, F.; Dodelet, J. *Science* **2009**, *324*, 71.

(28) Lu, Y.; Wang, L.; Preuß, K.; Qiao, M.; Titirici, M.-M.; Varcoe, J.; Cai, Q. *J. Power Sources* **2017**, *372*, 82.

(29) Peng, X.; Omasta, T.; Magliocca, E.; Wang, L.; Varcoe, J.; Mustain, W. *Angew. Chem.* **2019**, *131*, 1058.

(30) Sa, Y.; Seo, D.; Woo, J.; Lim, J.; Cheon, J.; Yang, S.; Lee, J.; Kang, D.; Shin, T.; Shin, H.; Jeong, H.; Kim, C.; Kim, M.; Kim, T.; Joo, S. *J. Am. Chem. Soc.* **2016**, *138*, 15046.

(31) Venna, S.; Jasinski, J.; Carreon, M. *J. Am. Chem. Soc.* **2010**, *132*, 18030.

(32) Banerjee, R.; Phan, A.; Wang, B.; Knobler, C.; Furukawa, H.; O'Keeffe, M.; Yaghi, O. *Science* **2008**, *319*, 939.

(33) Tang, J.; Salunkhe, R.; Liu, J.; Torad, N.; Imura, M.; Furukawa, S.; Yamauchi, Y. *J. Am. Chem. Soc.* **2015**, *137*, 1572.

(34) Li, Y.; Jia, B.; Fan, Y.; Zhu, K.; Li, G.; Su, C. *Adv. Energy Mater.* **2018**, *8*, 1702048.

(35) Furukawa, H.; Cordova, K. E.; O'Keeffe, M.; Yaghi, O. M. *Science* **2013**, *341*, 1230444.

(36) Zhao, Y.; Yang, L.; Chen, S.; Wang, X.; Ma, Y.; Wu, Q.; Jiang, Y.; Qian, W.; Hu, Z. *J. Am. Chem. Soc.* **2013**, *135*, 1201.

(37) Sharifi, T.; Hu, G.; Jia, X.; Wågberg, T. *ACS Nano* **2012**, *6*, 8904.

(38) Xia, B.; Yan, Y.; Li, N.; Wu, H.; Lou, X.; Wang, X. *Nat. Energy* **2016**, *1*, 15006.

(39) Wu, M.; Wang, K.; Yi, M.; Tong, Y.; Wang, Y.; Song, S. *ACS Catal.* **2017**, *7*, 6082.

(40) Chen, Y.; Wang, C.; Wu, Z.; Xiong, Y.; Xu, Q.; Yu, S.; Jiang, H. *Adv. Mater.* **2015**, *27*, 5010.

DOI: 10.1021/jacs.9b03561
J. Am. Chem. Soc. XXXX, XXX, XXX–XXX

(41) Li, Y.; Jia, B.; Fan, Y.; Zhu, K.; Li, G.; Su, C. *Adv. Energy Mater.* **2018**, *8*, 1702048.
(42) Behr, M.; Gaulding, E.; Mkhoyan, K.; Aydil, E. J. *J. Appl. Phys.* **2010**, *108*, 053303.
(43) Park, K.; Ni, Z.; Cote, A.; Choi, J.; Huang, R.; Uribe-Romo, F.; Chae, H.; O'Keeffe, M.; Yaghi, O. *Proc. Natl. Acad. Sci. U. S. A.* **2006**, *103*, 10186.
(44) Huang, X.; Lin, Y.; Zhang, J.; Chen, X. *Angew. Chem., Int. Ed.* **2006**, *45*, 1557.
(45) Meng, F.; Wang, Z.; Zhong, H.; Wang, J.; Yan, J.; Zhang, X. *Adv. Mater.* **2016**, *28*, 7948.
(46) Cliff, G.; Lorimer, G. *J. Microsc.* **1975**, *103*, 203.
(47) Singh, S.; Kashyap, V.; Manna, N.; Bhange, S.; Soni, R.; Boukherroub, R.; Szunerits, S.; Kurungot, S. *ACS Catal.* **2017**, *7*, 6700.
(48) Fu, G.; Yan, X.; Chen, Y.; Xu, L.; Sun, D.; Lee, J.; Tang, Y. *Adv. Mater.* **2018**, *30*, 1704609.
(49) Wu, M.; Wang, K.; Yi, M.; Tong, Y.; Wang, Y.; Song, S. *ACS Catal.* **2017**, *7*, 6082.
(50) Wang, Y.; Yang, Y.; Jia, S.; Wang, X.; Lyu, K.; Peng, Y.; Zheng, H.; Wei, X.; Ren, H.; Xiao, L.; Wang, J.; Muller, D.; Abruña, H.; Hwang, B.; Lu, J.; Zhuang, L. *Nat. Commun.* **2019**, *10*, 1506.
(51) Sun, J.; Lowe, S.; Zhang, L.; Wang, Y.; Pang, K.; Wang, Y.; Zhong, Y.; Liu, P.; Zhao, K.; Tang, Z.; Zhao, H. *Angew. Chem.* **2018**, *130*, 16749.
(52) Wang, J.; Liu, W.; Luo, G.; Li, Z.; Zhao, C.; Zhang, H.; Zhu, M.; Xu, Q.; Wang, X.; Zhao, C.; Qu, Y.; Yang, Z.; Yao, T.; Li, Y.; Lin, Y.; Wu, Y.; Li, Y. *Energy Environ. Sci.* **2018**, *11*, 3375.
(53) Li, S.; Cheng, C.; Liang, H.; Feng, X.; Thomas, A. *Adv. Mater.* **2017**, *29*, 1700707.
(54) Hu, C.; Dai, L. *Adv. Mater.* **2017**, *29*, 1604942.
(55) Xiang, Z.; Xue, Y.; Cao, D.; Huang, L.; Chen, J.; Dai, L. *Angew. Chem.* **2014**, *126*, 2465.
(56) Sethuraman, V.; Weidner, J.; Haug, A.; Motupally, S.; Protsailo, L. *J. Electrochem. Soc.* **2008**, *155*, B50.
(57) Kim, Y.; Moh, L.; Swager, T. *ACS Appl. Mater. Interfaces* **2017**, *9*, 42409.
(58) Gasteiger, H.; Kocha, S.; Sompalli, B.; Wagner, F. *Appl. Catal., B* **2005**, *56*, 9.

DOI: 10.1021/jacs.9b03561
J. Am. Chem. Soc. XXXX, XXX, XXX−XXX